

---

# XAI Benchmark for Visual Explanation

---

**Yifei Zhang**

Emory University  
Atlanta, GA 30322  
yifei.zhang2@emory.edu

**Siyi Gu**

Emory University  
Atlanta, GA 30322  
carrie.gu@emory.edu

**James Song**

Emory University  
Atlanta, GA 30322  
james.song2@emory.edu

**Bo Pan**

Emory University  
Atlanta, GA 30322  
bo.pan@emory.edu

**Liang Zhao\***

Emory University  
Atlanta, GA 30322  
liang.zhao@emory.edu

## Abstract

The rise of deep learning algorithms has led to significant advancements in computer vision tasks, but their "black box" nature has raised concerns regarding interpretability. Explainable AI (XAI) has emerged as a critical area of research aiming to open this "black box", and shed light on the decision-making process of AI models. Visual explanations, as a subset of Explainable Artificial Intelligence (XAI), provide intuitive insights into the decision-making processes of AI models handling visual data by highlighting influential areas in an input image. Despite extensive research conducted on visual explanations, most evaluations are model-centered since the availability of corresponding real-world datasets with ground truth explanations is scarce in the context of image data. To bridge this gap, we introduce an XAI Benchmark comprising a dataset collection from diverse topics that provide both class labels and corresponding explanation annotations for images. We have processed data from diverse domains to align with our unified visual explanation framework. We introduce a comprehensive Visual Explanation pipeline, which integrates data loading, preprocessing, experimental setup, and model evaluation processes. This structure enables researchers to conduct fair comparisons of various visual explanation techniques. In addition, we provide a comprehensive review of over 10 evaluation methods for visual explanation to assist researchers in effectively utilizing our dataset collection. To further assess the performance of existing visual explanation methods, we conduct experiments on selected datasets using various model-centered and ground truth-centered evaluation metrics. We envision this benchmark could facilitate the advancement of visual explanation models. The XAI dataset collection and easy-to-use code for evaluation are publicly accessible at <https://xaidataset.github.io>.

## 1 Introduction

Deep learning algorithms have demonstrated remarkable performance in various computer vision tasks, leading to their widespread adoption. However, the "black box" nature of Deep Neural Networks (DNNs) poses challenges in ensuring the interpretability and reasonableness of AI decisions [1, 45]. In response, Explainable AI (XAI) has gained significant importance as a field aimed at understanding the underlying rationales behind model decision-making, particularly in computer vision tasks [9, 36]. By providing interpretable explanations for computer vision tasks, XAI empowers users to comprehend

---

\*Corresponding author

and trust AI model decisions, thereby enhancing transparency, accountability, and the identification of potential biases or limitations. In particular, there are mainly three streams of approaches in the computer vision domain applying: 1) gradient-based methods, 2) perturbation-based methods, or 3) CAM-based methods, to obtain saliency maps that highlight sub-parts of an image that are most responsible for the model prediction [16, 21].

To be more specific, gradient-based methods utilize the concept of partial derivatives in the context of the model’s decision function. They compute the gradients of the model’s output with respect to each pixel in the input image. These gradients represent how much a small change in a particular pixel’s value will affect the model’s output. In recent years, there has been considerable advancement in the development of gradient-based attribution methods. Notable among these methods are Class Activation Mapping (CAM) [51], Gradient-weighted Class Activation Mapping (Grad-CAM) [39], Integrated Gradients [44], and Guided Backpropagation [43]. Another common type of explanation technique in XAI for image classification is the perturbation-based method. This strategy involves introducing deliberate alterations or perturbations to the input image and analyzing the resulting changes in the model’s predictions. By systematically adjusting specific regions or components of the image and observing the corresponding modifications in the model’s output, these methods reveal the key visual attributes that drive the model’s decision-making process. Through this process, perturbation-based methods provide valuable insights into the factors influencing the model’s predictions. A variety of methods such as Occlusion [49], Local Interpretable Model-Agnostic Explanations (LIME) [31], Randomized Input Sampling for Explanation of Black-box Models (RISE) [34], and Shapley Additive exPlanations (SHAP) [29] employ this approach.

Though image classification benchmark datasets such as MNIST, ImageNet, CIFAR-10, and CIFAR-100 can be utilized for visual explanation tasks, their effectiveness is curtailed. This is due to the absence of specific ground truth explanation annotations, which consequently limits the scope of the evaluation. The absence of such resources in the visual explanation domain poses significant challenges to the research of this domain, which can be summarized as follows: **1) Hindering Innovation and Evaluation:** Without these resources, both the development of new techniques and the evaluation of model effectiveness are impeded, as there’s no uniform platform or common reference for comparison. **2) Reproducibility, Verification, and Entry Barriers:** The lack of standardized datasets complicates the replication and validation of results, is critical for scientific progress, and presents a significant hurdle for newcomers, barring the initial research stages. **3) Real-world Applicability and Standardization Deficit:** Limited diversity in benchmark datasets potentially restricts the scope of model testing scenarios, risking the creation of models with limited real-world applicability. Moreover, the absence of agreed benchmarks hampers standardization, impeding meaningful comparisons across studies.

To address the challenges aforementioned, we introduce our Explainable Artificial Intelligence (XAI) Benchmark for Visual Explanation. An overview is shown in Figure 2. This collection amasses and processes a large number of image datasets with explanation annotations, covering a broad range of domains and subjects such as object classification, medical imaging classification, and prohibited item detection. Additionally, it standardizes the procedures for model evaluation and provides benchmark results across a multitude of datasets. The principal contributions of our work are as follows:

- We have published eight unique datasets that span a range of topics such as object classification, medical imaging classification, and prohibited item detection.
- We executed comprehensive experiments employing four publicly available datasets. These encompassed an array of visual explanation models, employed both model-centered and ground-truth-centered metrics for evaluation, and were followed by an in-depth analysis of the results.
- We have developed a user-friendly API to streamline the process of accessing and leveraging pre-processed datasets. Additionally, we have provided easily accessible, ready-to-use code for a variety of evaluation metrics on our website.

## 2 Related Work

Because of the significant importance of XAI in explaining rationales of DNNs, many benchmarks such as XAI-Bench [27], OpenXAI [2], SHAPEGGEN [3], ERASER [13], and CLEVR-XAI [5], have been proposed for various types of data including tabulations, graphs, texts, and images. XAI-Bench is a collection of synthetic datasets with known ground truth distributions that enables the

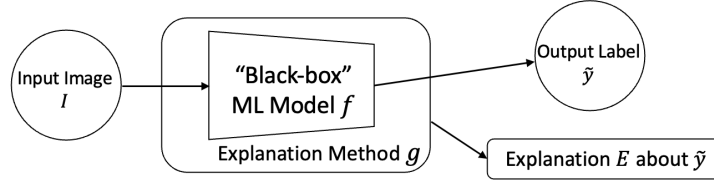


Figure 1: Illustration of Visual Explanation Models: Using the Explanation Method  $g$  to Explain the Decision  $\hat{y}$  of "Black-Box" Machine Learning Model  $f$ .

computations of evaluation metrics and thus the evaluations of feature attribution methods [27]. In contrast, OpenXAI takes one step further: besides featuring a synthetic data generator, OpenXAI also provides more evaluation metrics and 7 real-world datasets [2]. Similar to XAI-Bench and OpenXAI, SHAPEGGEN is another synthetic dataset generator with ground truth explanations for benchmarking graph neural network (GNN) explainers [3]. On the other hand, ERASER is a Natural Language Processing (NLP) benchmark consisting of repurposed and augmented corpora with human-annotated rationales for decisions [13]. In the NLP domain, there are several works regarding evaluating model-generated rationale against human-annotated rationale [19, 8, 10] using metrics such as ROUGE, BLEU, as well as sufficiency-accuracy. And CLEVR-XAI is a benchmark focused on evaluating visual explanations of Visual Question Answering (VQA) tasks with questions and ground truth masks, which is adapted from Compositional Language and Elementary Visual Reasoning (CLEVR) diagnostics dataset [5, 22]. Specifically on XAI involving images, extensive work has also been done. Popular methods of generating interpretable explanations include two major approaches: CAM [51], Grad-CAM [39], integrated Gradients [35], Guided Backpropagation [32], etc. which use gradient-based attribution, and LIME [31], RISE [34], SHAP [29], etc. which use perturbation-based analysis. Many image datasets have also been proposed and used to test these methods. Additionally, there exist causality-based techniques for visual explanation [50, 47, 28]. However, these methods consistently rely on synthetic images with various factors as prior knowledge. ImageNet Large Scale Visual Recognition Challenge (ILSVRC) [38] is a benchmark for object detection and classification with millions of images [51]. The Pascal VOC 2012 is another dataset for object recognition [11]. Other similar datasets include MNIST, CIFAR-10, CIFAR-100, etc. are also popular datasets used for image classification. However, those image datasets often lack the use of ground-truth-centered evaluations due to the absence of benchmarks with ground-truth annotations [46]. Existing evaluations of visual explanation methods still rely on surveys or questionnaires [39, 34, 14] from human judgment without task-specific criteria. [18, 39] introduced User Interfaces (UIs) to evaluate visual explanations based on human readability. Unlike the NLP field, where textual rationales are easily gathered from platforms like forums [8, 48, 23], sourcing rationales for image data is more challenging. Although image datasets with explanations have been suggested, they lack standardized benchmarks.

### 3 Visual Explanation

Visual explanation employs visual representations to clarify and interpret intricate concepts, systems, or data. Within the realm of artificial intelligence (AI), visual explanations are vital for elucidating the reasoning behind an AI model's decision or output and pinpointing the significant factors within the input data that contributed to such a decision.

In the domain of image classification, a visual explanation typically takes the form of a saliency map  $E$  superimposed on the input image  $I$ , highlighting the regions that were most influential for the classifier  $f$  in making its decision, as exemplified in Figure 1. For instance, if the model is classifying animal images, the heatmap may reveal that the model focused on specific features such as the shape of the animal's nose or the pattern of its fur to determine the animal's category. Formally, the visual explanation problem can be defined as the function  $g$  that maps the input image  $I$  and the classifier  $f$  to an importance map  $E$ , denoted as  $g : (I, f) \rightarrow E$ . The importance map  $E$  shares the same dimensions as  $I$  and assigns an importance score to each pixel of the image.

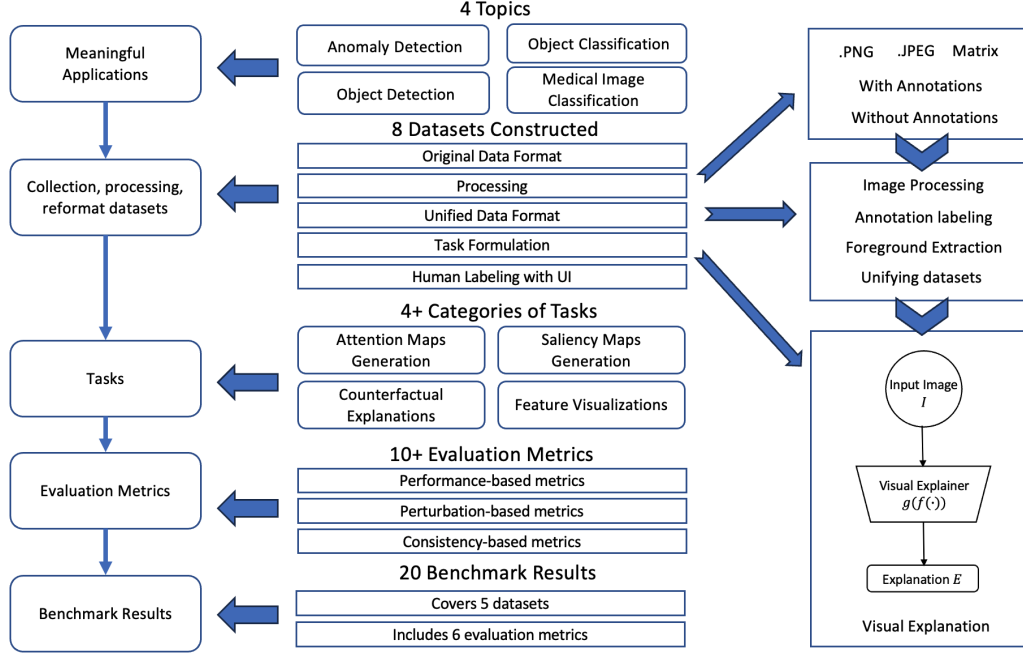


Figure 2: Overview of XAI Benchmark for Visual Explanation.

Dataset	Class Type	Size	Annotation Type	Format	Balanced	Counterfactual
Gender Classification	Binary	1,736	Human annotation	Pixel-wise	✓	✓
Scene Recognition	Binary	2,086	Human annotation	Pixel-wise	✓	✓
Face Glasses Recognition	Binary	885	Human annotation	Pixel-wise	✓	✗
Prohibited Item Detection	Binary	1,059,231	Human annotation	Bounding-box	✗	✗
Nodule Detection	Binary	2,625	Human annotation	Pixel-wise	✗	✗
Tumor Detection	Binary	281	Human annotation	Pixel-wise	✗	✗
Cats and Dogs Classification	Multi-class	7,349	Foreground segmentation	Pixel-wise	✓	✗
Object Classification	Multi-class	11,540	Foreground segmentation	Pixel-wise	✓	✗

Table 1: Summary of Currently Available Datasets: The column labeled "Class Type" indicates the number of classes included in each dataset. "Size" describes the total count of images, class labels, and explanation annotation pairs within the dataset. "Annotation Type" delineates the source of the explanation annotations. "Format" specifies the manner in which the explanation annotations are presented. The "Balanced" column signifies whether the dataset maintains balance in terms of the predictive label, while the "Counterfactual" column indicates the provision of counterfactual explanation annotations.

## 4 Description of collected datasets

Our current version of dataset collection consists of eight real-world datasets, with each of them containing images with their class labels and ground truth explanation annotations. These datasets serve as benchmarks for visual explanation research, providing valuable resources for researchers in this field. Table 4 presents an overview of these datasets, presenting essential information for researchers interested in utilizing them for their investigations. The subsequent sections provide detailed descriptions of each dataset, including the specific data processing procedures employed. For classification tasks where the objective is to locate and identify an object, we use segmentation masks as our ground-truth explanation. For classification tasks where the decision-making process relies on the characteristics of an object instead of the whole object, we employ human annotation user interfaces(UIs) and asks annotators to manually highlight the region that is critical to the classification result.

**Gender Classification Dataset (Gender)** The gender classification task utilized in our study is derived from the Microsoft COCO dataset [26], which is available at <https://cocodataset.org/>.

To construct the task-specific dataset, we extracted images from the COCO dataset that contained captions with the terms "men" or "women". Further filtering was performed to remove images that had both genders mentioned in the caption, multiple individuals present, or depicted as unrecognizable humans. Moreover, a subset of the images underwent manual annotation by human annotators, resulting in factual and counterfactual masks that indicate binary labels of positive and negative, respectively. The human annotation labels were acquired using human annotation user interfaces (UIs) for both annotation and evaluation purposes [17, 18]. The dataset comprises a total of 1,736 images, evenly distributed between female and male annotations.

**Scene Recognition Dataset (Scene)** The scene recognition dataset used in our study is derived from the Places365 dataset, which can be accessed at <http://places2.csail.mit.edu/index.html> [52]. The dataset was further annotated manually by Gao et al. [17, 18] with human annotation user interfaces (UIs) to obtain factual and counterfactual masks. The task of this dataset involves binary classification for scene recognition, specifically distinguishing between nature and urban scenes. To create the dataset, specific categories were selected for sampling, including nature categories. Specifically, the categories used to sample the data are: *Nature*: mountain, pond, waterfall, field wild, forest broadleaf, rainforest *Urban*: house, bridge, campus, tower, street, driveway In total, the dataset comprises 2,086 images, each annotated with human explanation labels.

**Face Glasses Recognition Dataset** The glasses recognition dataset utilized in our study is derived from the CelebAMask-HQ dataset, which can be accessed at [http://mmlab.ie.cuhk.edu.hk/projects/CelebA/CelebAMask\\_HQ.html](http://mmlab.ie.cuhk.edu.hk/projects/CelebA/CelebAMask_HQ.html) [25]. The dataset is initially categorized by distinguishing face images with and without glasses. The CelebAMask-HQ dataset includes manually annotated masks with 19 classes covering various facial components and accessories. Using the segmentation of eyes and glasses, we derive factual labels for recognizing glasses. The dataset includes 885 images, each with corresponding explanation annotations.

**Prohibited Item Detection Dataset** The prohibited item detection task in our study is constructed using the Sixray dataset, available online at <https://github.com/MeioJane/SIXray> [30]. The dataset is partitioned by categorizing images based on the presence of prohibited items. The Sixray dataset encompasses a vast collection of 1,059,231 X-ray images, accompanied by image-level explanation annotations provided by human security inspectors. These annotations cover six classes, encompassing a total of 8,929 prohibited items. For the purpose of our task, the six prohibited classes are merged, resulting in a binary prohibited item detection problem. All images in the dataset include bounding box annotations for the prohibited items.

**Nodule Detection Dataset (Nodule)** We construct the nodule detection dataset from LIDC-IDRI [4] which consists of lung cancer screening thoracic computed tomography (CT) scans with marked-up annotated lesions. We preprocess the 3D nodule images into 2D images by taking the middle slice along the z-axis and keeping the dimension as  $224 \times 224$ . Annotations are from at most four experienced thoracic radiologists in XML format. We obtain ground truth explanation by computing the consensus volume amongst the provided four annotations corresponding to each image at a 50% consensus level. After locating the nodules, we further slice surrounding areas as our negative samples. The dataset after preprocessing includes 2625 nodules and 65505 non-nodule images. We use this dataset with the objective to determine whether an image includes a nodule or not.

**Tumor Detection Dataset (Tumor)** To construct our dataset, we sourced normal pancreas images from the Cancer Imaging Archive, accessible online at <https://wiki.cancerimagingarchive.net/display/Public/Pancreas-CT> [37]. Abnormal images were obtained from the Medical Segmentation Decathlon dataset (MSD). The dataset comprises 281 scans with tumors and 80 scans without tumors. To preprocess the data, we transformed it into 2D images by randomly selecting a slice along the z-axis. Within the MSD dataset, two types of annotations are available: tumor lesions and pancreas segmentation. In our study, we considered the tumor lesions as our explanation labels.

**Cats and Dogs Classification Dataset (Cat and Dog)** The Cats and Dogs Classification Dataset used in our study is constructed from The Oxford-IIIT Pet Dataset, which is accessible at <https://www.robots.ox.ac.uk/~vgg/data/pets/> [33]. Designed specifically for pet image analysis tasks, this dataset comprises more than 7,000 images spanning 37 distinct categories, all representing various breeds of dogs or cats. Each image is meticulously annotated with pixel-level trimap segmentation ground truth. Serving as a crucial asset, the Oxford-IIIT Pet Dataset plays a pivotal role in training and assessing computer vision models within the pet image analysis domain. Within



Figure 3: Row (a): Images from object classification datasets; Row (b): The visual explanation outputs obtained from GradCAM trained with RESNET-18 classifier (the heatmaps are up-sampled to fit the size of the original image); Row (c): The corresponding ground truth annotation masks.

our study, explanation annotations were derived by extracting pixel-level foreground segmentation corresponding to the image’s label class.

**Object Classification Dataset (Object)** The Object Classification Dataset utilized in our study is constructed from the PASCAL VOC 2012 Dataset, which can be accessed at <http://host.robots.ox.ac.uk/pascal/VOC/voc2012/> [15]. The PASCAL VOC 2012 Dataset is an extensive collection of images that covers 20 diverse object categories. These include *cars, dogs, chairs, people, bicycles, cats, horses, birds, boats, aeroplanes, buses, trains, motorcycles, cows, dining tables, potted plants, sheep, sofas, TVs, and bottles*. Each image within the dataset is manually annotated with object bounding boxes, pixel-level segmentation masks, and corresponding class labels for the identified objects. The VOC 2012 Dataset comprises approximately 11,540 images, providing a diverse and extensive resource for object classification research. In our study, the explanation annotations were generated by extracting pixel-level foreground segmentation corresponding to the image label class. Examples are shown in Table 3.

## 5 Evaluation Metric

Our benchmark provides easily accessible code implementations for a comprehensive collection of quantitative metrics proposed by previous research. These metrics are designed to assess the faithfulness, stability, and fairness of visual explanation methods. We categorize these metrics into three classes: 1) Performance-based metrics 2) Perturbation-based metrics, and 3) Consistency-based metrics. A detailed description of these metrics is provided below.

### 5.1 Performance-based metrics

Performance-based metrics are quantitative indicators primarily focusing on the predictive accuracy of the model. These metrics, including IoU, precision, recall, F1-score, and Pointing Game, assess how effectively the model accomplishes the task it was trained for, regardless of the interpretability aspect. Additionally, these metrics are ground truth-centered evaluations that rely on subjective evaluations from human experts who scrutinize various facets of the model’s visual explanations based on their knowledge and critical judgment.

**Intersection over Union (IoU):** IoU is a metric commonly used to measure the overlap between the predicted and ground truth annotations. It quantifies the extent to which the predicted region aligns with the true region. The IoU is calculated as the ratio of the intersection of the predicted and ground truth regions to their union: 
$$\text{IoU} = \frac{\text{True Positive}}{\text{True Positive} + \text{False Positive} + \text{False Negative}} \quad [7].$$

**Precision, Recall, F1:** Precision assesses the proportion of correctly predicted positive instances out of all instances predicted as positive. It measures the accuracy of positive predictions. Precision is calculated as:  $\text{Precision} = \frac{\text{True Positive}}{\text{True Positive} + \text{False Positive}}$ . Recall, also known as sensitivity or true positive rate, measures the proportion of correctly predicted positive instances out of all actual positive instances. It captures the model’s ability to identify positive instances correctly. Recall is calculated as:  $\text{Recall} = \frac{\text{True Positive}}{\text{True Positive} + \text{False Negative}}$ . F1 takes into account of both precision and recall and is calculated as  $\text{F1} = 2 \times \frac{\text{Precision} * \text{Recall}}{\text{Precision} + \text{Recall}}$ .

**Pointing Game:** The idea of the Pointing Game is that if the most important region of the image (as identified by the explanation) contains the object of interest, the explanation is considered correct. This is calculated as a success rate over a dataset. To be more specific, if the highest saliency point lies inside the human-annotated bounding box of an object, it is counted as a hit, otherwise counted as a miss. The pointing game accuracy is given by  $\text{Accuracy} = \frac{\#Hits}{\#Hits + \#Misses}$  [34].

## 5.2 Perturbation-based metrics

Perturbation-based metrics, including The Average Drop % score, Deletion, Insertion, and Adversarial perturbation, are a type of causal-based model-centered evaluation method. These metrics gauge the influence of modifications in the input data, such as the addition, deletion, or alteration of features, on the model’s output. The causal nature of these metrics lies in their capacity to elucidate the cause-and-effect relationship between the input features and the model’s decisions. They aid in comprehending the significance of various features in the decision-making process of the model, thus enabling a better understanding of the model’s behavior and logic. By evaluating how the model’s output is affected by intentional perturbations of specific input features, these metrics provide insights into the causal dependencies within the model.

**The Average Drop % score:** The Average Drop % score assesses the significance of regions highlighted by visual explanation methods. It quantifies the decrease in a model’s performance when these identified regions are masked. A significant drop indicates that the highlighted regions in the image are vital for the model’s decisions. This metric helps validate the effectiveness of visual explanations, ensuring the pinpointed areas in images genuinely influence the model’s predictions [11].

**Deletion:** Deletion is a way of testing how much the prediction score changes when you remove the most important features, as identified by the explanation. In the context of image classification, for example, you’d remove (or occlude) the most important parts of the image and see how much the model’s confidence in its prediction decreases. Formally, the Deletion metric  $D$  can be calculated as:  $D = \frac{1}{N} \sum_{r=1}^N S(f(I \odot M_{>r}))$ , where  $\odot$  denotes element-wise product,  $N$  is the number of pixels,  $M_{>r}$  is a binary mask that masks the  $r$  most important pixels, and  $S$  is the model’s prediction score, and  $r$  is the rank of a pixel according to the explanation method.

**Insertion:** Insertion tests how much the prediction score changes when you add the most important features, starting from a blank image. You gradually insert the most important parts of the image, as identified by the explanation, and see how much the model’s confidence in its prediction increases. If the explanation is good, then inserting the parts of the image it highlights should increase the prediction confidence significantly. Formally, The Insertion metric  $I$  can be calculated as  $I = \frac{1}{N} \sum_{r=1}^N S(f(I \odot M_{\leq r}))$ , where  $M_{\leq r}$  is a binary mask that reveals only  $r$  most important pixels.

**Adversarial perturbation:** Adversarial perturbations involve subtly modifying input data in a way that is almost imperceptible to humans but leads to significant changes in the model’s output or prediction. By identifying which features are most susceptible to these perturbations, we can gain insight into the features that the model deems important for decision-making [16].

**Sufficiency and Comprehensiveness:** These are explanation evaluation techniques widely used in the NLP domain, which measure whether a rationale is sufficient/necessary for a model’s prediction by comparing the model’s prediction score on the full input with prediction score on masked input. The two metrics are often applied together to jointly measure the explanation’s fidelity. The comprehensiveness and sufficiency score can be calculated as  $C = f(I) - f(I \odot M_{\leq k})$  and  $S = f(I) - f(I \odot M_{>k})$  where  $M_{(\cdot)}$  denotes the binary mask obtained from the given explanation method with a threshold  $k$ .

### 5.3 Consistency-based metrics

Existing works also propose consistency-based evaluation to measure how well the explanation aligns across similar instances [6, 42]. It measures the similarity of explanations of similar instances given the assumption that model explanations should be similar between very similar inputs. This metric is first used in the NLP domain and we generalize the metric as follows. Data Consistency =  $|g(f(I)) - g(f(I \odot M))|$ , where  $M$  is a random mask that masks out  $k$  input features from  $I$  and  $g$  is the model generated explanation.  $k$  will be treated as a hyper-parameter depending on the dataset. Formally,  $M$  is a binary mask vector of the same size as  $I$  (say,  $n$ ), and  $\sum_{i=1}^n M[i] = n - k$ , where  $M[i]$  denotes the  $i$ -th element of the mask  $M$ .

## 6 Benchmark Experiments

In this section, we describe how we benchmark state-of-the-art visual explanation methods with published datasets. We choose eight common visual explanation methods. For Activation-based Methods, we choose CAM [51], GradCAM [39], GradCAM++ [11]. For Gradient-based Methods, we choose IntegratedGradients [44], GuidedBackpropagation [32], Saliency [41], and Input X Gradient [40]. For the Perturbation-based method, we choose RISE [34]. We also discuss the key findings of this benchmarking analysis.

### 6.1 Experimental Setup and Preparation

We utilize the ResNet18 architecture [20] pre-trained on ImageNet [12] as our image classifier, fine-tuning the final fully connected layer to accommodate the class count in our target dataset. Default hyperparameter settings are employed for the visual explanation models, following the guidelines provided in the original implementations. The models undergo 30 epochs of training using the Adam optimizer [24] with a learning rate of 0.0001. All experiments are conducted on Amazon EC2 g4dn.xlarge instances, which are equipped with NVIDIA Tesla T4 GPUs.

Dataset	Accuracy	Precision	Recall	F1-score
Gender	0.7420	0.7416	0.7413	0.7415
Scene	0.9440	0.9441	0.9438	0.9439
Cat and Dog	0.9814	0.9817	0.9814	0.9813
Object-1	0.8712	0.8715	0.8712	0.8713
Object-2	0.7712	0.8171	0.7712	0.7847

Table 2: Classification Performance.

We assess the visual explanation methods’ performance using four ground-truth-centered evaluation metrics: IoU, Precision, Recall, and Pointing Game. These metrics are used to compare the generated explanations against our proposed ground truth. Additionally, we employ two model-centered evaluation metrics, insertion, and deletion, for evaluations without relying on ground truth. Our benchmark evaluation encompasses the Gender, Scene, Cat and Dog, and Object datasets.

In the case of the Object dataset, which consists of multiple classes, we conduct two distinct experiments. The first experimental study concentrated on three distinct classes, namely bird, horse, and sheep, collectively termed Object-1. The dataset encapsulating Object 1 comprised a total of 765 samples. A second experiment was designed around three different classes: aeroplane, car, and bus, collectively referred to as Object 2. This second experimental set, Object-2, consisted of 795 samples in total. For each of these experimental investigations, the sample allocation was divided as follows: 60% of the total samples were employed for the training phase, 20% were used for validation, and the remaining 20% were reserved for the testing phase.

### 6.2 Result and Analysis

The evaluation process commences with an assessment of the performance of the trained classifier on each respective dataset. The outcomes of these classifications for each experiment are comprehensively presented in Table 6.1. Then we evaluate the visual explanation methods on each dataset with a variety of performance-based metrics (IoU, Precision, Recall, and Pointing Game) and perturbation-based metrics (Insertion and Deletion). We further provide a qualitative analysis of the Cat and Dog dataset, presented in the supplementary section.



**Quantitative Analysis** From Table 6.2, we can observe that RISE outperforms CAM, Grad-CAM, GradCAM++, IntegratedGradients (IG), GuidedBackpropagation (GBP), InputXGradient, and Saliency in most of the datasets. Notably, RISE takes advantage of its model-agnostic nature, its ability to provide a global interpretation of the model’s decisions, its inherent robustness, and its potential to better handle multi-modal inputs. Its strategy of aggregating predictions over multiple randomly sampled binary masks could lead to more stable and reliable explanations. Additionally, those methods CAM, GradCAM, and GradCAM++ that leverage hooking mechanisms work well on Pointing Game over rest methods. We believe that their feature of hooking mechanisms to tap into intermediate layers of the network, allowing them to capture more localized, high-resolution feature information, makes them particularly effective in the Pointing Game, which requires precise localization of the regions most responsible for the model’s prediction, therefore, enhancing their performance in this task. We believe that their feature of hooking mechanisms to tap into intermediate layers of the network matches with the Pointing Game’s focus on precise localization of the regions most responsible for the model’s prediction. This feature enables them to capture more localized, high-resolution feature information, thus making them particularly effective in the Pointing Game. The observed result might be attributed to the differing assessment focuses of the Pointing Game and metrics like IoU, Precision, and Recall. While the Pointing Game concentrates on pinpoint accuracy, IoU, Precision, and Recall to evaluate the comprehensive coverage of the object. Consequently, a method might excel at identifying a vital portion of the object but may not be as effective in encompassing the entire object. We observe that for perturbation-based evaluation metrics like insertion and deletion, which don’t necessitate ground truth annotations, RISE consistently demonstrates superior performance compared to other models. This performance improvement is notable even when compared against aligned evaluation methods that utilize our proposed ground truth annotations.

## 7 Conclusion and Limitation

Our work entails the release of an XAI benchmark for the visual explanation that consists of eight distinct datasets across topics like object classification and medical imaging. Comprehensive experiments were carried out on four datasets, applying various visual explanation models and evaluation metrics. This thorough analysis offered valuable insights into model performance and interpretability. To aid users, we created an API for simplified dataset access and made easy-to-use evaluation metric code available on our website, enhancing ease in assessing visual explanation methods. These efforts aim to foster advancement and further research in explainable AI.

While our work addresses the absence of ground truth explanation annotations for visual explanation model evaluations, we note a few possible limitations of our proposed benchmark. For example, for two of our proposed datasets, namely Gender Classification and Scene Recognition, the ground-truth explanation annotations are acquired through human labeling. Despite our incorporation of multiple annotators and the adoption of a majority vote strategy, there remains the possibility of bias stemming from annotators’ individual characteristics. Also, regarding the pancreatic tumor detection dataset, the negative and positive samples are sourced from different sources. This situation introduces a potential bias wherein the classifiers could inadvertently learn to predict the image source—a variable inherently aligned with the label—instead of focusing on the crucial causal information, such as the tumor’s actual location.

Dataset	Model	IoU	Precision	Recall	Pointing	Insertion	Deletion
Gender	GradCAM	0.1304	0.5371	0.5677	0.2901	0.696	0.129
	CAM	0.1429	0.5396	0.5577	0.3077	<u>0.688</u>	<u>0.123</u>
	GradCAMpp	0.1417	0.5379	0.5644	0.2906	0.663	0.152
	IG	<u>0.3441</u>	<u>0.7939</u>	0.7232	0.2138	0.363	0.252
	GBP	<b>0.3542</b>	<b>0.8076</b>	<b>0.7343</b>	0.2931	0.397	0.228
	InputXGradient	0.3403	0.6345	0.6712	0.3011	0.401	0.248
	Saliency	0.3229	0.7831	0.6620	<u>0.3208</u>	0.381	0.233
	RISE	0.3416	0.7875	<u>0.7285</u>	<b>0.3307</b>	<b>0.845</b>	<b>0.101</b>
Scene	GradCAM	0.3656	0.7637	0.5096	<b>0.4777</b>	0.691	0.110
	CAM	0.3704	0.7625	0.4988	0.3852	<u>0.711</u>	<b>0.103</b>
	GradCAMpp	0.3632	0.7637	0.4977	<u>0.4224</u>	0.701	<u>0.104</u>
	IG	<u>0.5356</u>	0.8144	0.6368	<u>0.2810</u>	0.511	0.201
	GBP	0.4832	0.8456	0.5842	0.3277	0.582	0.211
	InputXGradient	0.4566	0.8272	<b>0.7043</b>	0.3010	0.572	0.226
	Saliency	0.5104	<u>0.8523</u>	0.6612	0.3100	0.491	0.206
	RISE	<b>0.5428</b>	<b>0.8675</b>	0.6674	0.3624	<b>0.923</b>	0.109
Cat and Dog	GradCAM	0.1599	0.1641	0.8116	<u>0.3121</u>	0.752	0.343
	CAM	0.1284	0.1285	0.8437	<u>0.3121</u>	0.736	0.378
	GradCAMpp	0.1236	0.1239	0.8349	<b>0.3434</b>	0.766	0.351
	IG	0.3002	0.3003	<u>0.9974</u>	0.1728	0.399	<u>0.270</u>
	GBP	<u>0.3026</u>	0.3029	0.9973	0.2184	0.472	0.301
	InputXGradient	0.2808	<u>0.3062</u>	0.9244	0.1892	0.468	0.317
	Saliency	0.2978	0.3049	0.9741	0.2136	0.422	0.290
	RISE	<b>0.3094</b>	<b>0.3095</b>	<b>0.9987</b>	0.1628	<b>0.886</b>	<b>0.236</b>
Object-1	GradCAM	0.0518	0.0518	0.3808	<u>0.1993</u>	<u>0.667</u>	0.351
	CAM	0.0524	0.0527	0.3731	<u>0.1667</u>	0.613	0.374
	GradCAMpp	0.0515	0.0516	0.3664	0.1933	0.629	0.378
	IG	0.1389	0.3395	<u>0.4998</u>	<b>0.2000</b>	0.397	<u>0.214</u>
	GBP	0.1250	0.3252	0.4918	0.1382	0.440	0.283
	InputXGradient	0.1312	<b>0.3553</b>	0.4010	0.1640	0.433	0.291
	Saliency	<b>0.1445</b>	0.3287	0.4299	0.1301	0.303	0.217
	RISE	<u>0.1423</u>	<u>0.3423</u>	<b>0.5266</b>	0.1400	<b>0.857</b>	<b>0.211</b>
Object-2	GradCAM	0.0527	0.0529	0.3719	<b>0.1976</b>	0.688	0.396
	CAM	0.0528	0.0529	0.3719	<u>0.1975</u>	0.692	0.401
	GradCAMpp	0.0533	0.0533	0.3708	<b>0.1976</b>	0.699	0.398
	IG	0.1472	<u>0.1491</u>	0.9263	0.1854	0.375	<b>0.211</b>
	GBP	0.1486	0.1486	0.9370	0.1882	0.510	0.253
	InputXGradient	0.1312	0.1442	0.9344	0.1929	0.482	<u>0.241</u>
	Saliency	<b>0.1672</b>	0.1485	<b>0.9627</b>	0.1704	0.375	<b>0.211</b>
	RISE	<u>0.1586</u>	<b>0.1595</b>	<u>0.9373</u>	0.1881	<b>0.836</b>	0.288

Table 3: Quantitative evaluation and comparison of visual explanation models on published datasets. The best results for each task are bolded and the second bests are underlined.

## References

- [1] A. Adadi and M. Berrada. Peeking inside the black-box: a survey on explainable artificial intelligence (xai). *IEEE access*, 6:52138–52160, 2018.
- [2] C. Agarwal, S. Krishna, E. Saxena, M. Pawelczyk, N. Johnson, I. Puri, M. Zitnik, and H. Lakkaraju. Openxai: Towards a transparent evaluation of model explanations, 2023.
- [3] C. Agarwal, O. Queen, H. Lakkaraju, and M. Zitnik. Evaluating explainability for graph neural networks, 2023.
- [4] S. G. Armato III, G. McLennan, L. Bidaut, M. F. McNitt-Gray, C. R. Meyer, A. P. Reeves, B. Zhao, D. R. Aberle, C. I. Henschke, E. A. Hoffman, et al. The lung image database consortium (lidc) and image database resource initiative (idri): a completed reference database of lung nodules on ct scans. *Medical physics*, 38:915–931, 2011.
- [5] L. Arras, A. Osman, and W. Samek. Clevr-xai: A benchmark dataset for the ground truth evaluation of neural network explanations. *Information Fusion*, 81:14–40, 2022. ISSN 1566-2535. doi: <https://doi.org/10.1016/j.inffus.2021.11.008>. URL <https://www.sciencedirect.com/science/article/pii/S1566253521002335>.

- [6] P. Atanasova, J. G. Simonsen, C. Lioma, and I. Augenstein. Diagnostics-guided explanation generation. In *Proceedings of the AAAI Conference on Artificial Intelligence*, volume 36, pages 10445–10453, 2022.
- [7] E. Bochinski, T. Senst, and T. Sikora. Extending iou based multi-object tracking by visual information. In *2018 15th IEEE International Conference on Advanced Video and Signal Based Surveillance (AVSS)*, pages 1–6. IEEE, 2018.
- [8] J. Boyd-Graber, S. Carton, S. Feng, Q. V. Liao, T. Lombrozo, A. Smith-Renner, and C. Tan. Human-centered evaluation of explanations. In *Proceedings of the 2022 Conference of the North American Chapter of the Association for Computational Linguistics: Human Language Technologies: Tutorial Abstracts*, pages 26–32, 2022.
- [9] V. Buhrmester, D. Münch, and M. Arens. Analysis of explainers of black box deep neural networks for computer vision: A survey. *Machine Learning and Knowledge Extraction*, 3: 966–989, 2021.
- [10] S. Carton, A. Rathore, and C. Tan. Evaluating and characterizing human rationales. *arXiv preprint arXiv:2010.04736*, 2020.
- [11] A. Chattopadhyay, A. Sarkar, P. Howlader, and V. N. Balasubramanian. Grad-cam++: Generalized gradient-based visual explanations for deep convolutional networks. In *2018 IEEE winter conference on applications of computer vision (WACV)*, pages 839–847. IEEE, 2018.
- [12] J. Deng, W. Dong, R. Socher, L.-J. Li, K. Li, and L. Fei-Fei. Imagenet: A large-scale hierarchical image database. In *2009 IEEE conference on computer vision and pattern recognition*, pages 248–255. Ieee, 2009.
- [13] J. DeYoung, S. Jain, N. F. Rajani, E. Lehman, C. Xiong, R. Socher, and B. C. Wallace. Eraser: A benchmark to evaluate rationalized nlp models, 2020.
- [14] F. Doshi-Velez and B. Kim. Towards a rigorous science of interpretable machine learning. *arXiv preprint arXiv:1702.08608*, 2017.
- [15] M. Everingham, L. Van Gool, C. K. I. Williams, J. Winn, and A. Zisserman. The pascal visual object classes (voc) challenge. *International Journal of Computer Vision*, 88:303–338, June 2010.
- [16] Y. Gao, S. Gu, J. Jiang, S. R. Hong, D. Yu, and L. Zhao. Going beyond xai: A systematic survey for explanation-guided learning. *arXiv preprint arXiv:2212.03954*, 2022.
- [17] Y. Gao, T. S. Sun, G. Bai, S. Gu, S. R. Hong, and Z. Liang. RES: A robust framework for guiding visual explanation. In *Proceedings of the 28th ACM SIGKDD Conference on Knowledge Discovery and Data Mining*. ACM, aug 2022. doi: 10.1145/3534678.3539419. URL <https://doi.org/10.1145/3534678.3539419>.
- [18] Y. Gao, T. S. Sun, L. Zhao, and S. R. Hong. Aligning eyes between humans and deep neural network through interactive attention alignment. *Proceedings of the ACM on Human-Computer Interaction*, pages 1–28, 2022.
- [19] C. Garbacea and Q. Mei. Neural language generation: Formulation, methods, and evaluation. *arXiv preprint arXiv:2007.15780*, 2020.
- [20] K. He, X. Zhang, S. Ren, and J. Sun. Deep residual learning for image recognition. In *Proceedings of the IEEE conference on computer vision and pattern recognition*, pages 770–778, 2016.
- [21] M. Ivanovs, R. Kadikis, and K. Ozols. Perturbation-based methods for explaining deep neural networks: A survey. *Pattern Recognition Letters*, 150:228–234, 2021.
- [22] J. Johnson, B. Hariharan, L. van der Maaten, L. Fei-Fei, C. Lawrence Zitnick, and R. Girshick. Clevr: A diagnostic dataset for compositional language and elementary visual reasoning. In *Proceedings of the IEEE Conference on Computer Vision and Pattern Recognition (CVPR)*, July 2017.

- [23] D. Khashabi, S. Chaturvedi, M. Roth, S. Upadhyay, and D. Roth. Looking beyond the surface: A challenge set for reading comprehension over multiple sentences. In *Proceedings of the 2018 Conference of the North American Chapter of the Association for Computational Linguistics: Human Language Technologies, Volume 1 (Long Papers)*, pages 252–262, 2018.
- [24] D. P. Kingma and J. Ba. Adam: A method for stochastic optimization. *arXiv preprint arXiv:1412.6980*, 2014.
- [25] C.-H. Lee, Z. Liu, L. Wu, and P. Luo. Maskgan: Towards diverse and interactive facial image manipulation. In *IEEE Conference on Computer Vision and Pattern Recognition (CVPR)*, 2020.
- [26] T. Lin, M. Maire, S. J. Belongie, L. D. Bourdev, R. B. Girshick, J. Hays, P. Perona, D. Ramanan, P. Dollár, and C. L. Zitnick. Microsoft COCO: common objects in context. *CoRR*, abs/1405.0312, 2014. URL <http://arxiv.org/abs/1405.0312>.
- [27] Y. Liu, S. Khandagale, C. White, and W. Neiswanger. Synthetic benchmarks for scientific research in explainable machine learning, 2021.
- [28] Á. P. Martínez and J. V. Marca. Explaining visual models by causal attribution. in 2019 IEEE. In *CVF International Conference on Computer Vision Workshop (ICCVW)*, pages 4167–4175, 2019.
- [29] A. Messalas, Y. Kanellopoulos, and C. Makris. Model-agnostic interpretability with shapley values. In *2019 10th International Conference on Information, Intelligence, Systems and Applications (IISA)*, pages 1–7. IEEE, 2019.
- [30] C. Miao, L. Xie, F. Wan, C. Su, H. Liu, J. Jiao, and Q. Ye. Sixray : A large-scale security inspection x-ray benchmark for prohibited item discovery in overlapping images, 2019.
- [31] S. Mishra, B. L. Sturm, and S. Dixon. Local interpretable model-agnostic explanations for music content analysis. In *ISMIR*, volume 53, pages 537–543, 2017.
- [32] S. Mostafa, D. Mondal, M. A. Beck, C. P. Bidinosti, C. J. Henry, and I. Stavness. Leveraging guided backpropagation to select convolutional neural networks for plant classification. *Frontiers in Artificial Intelligence*, 5:871162, 2022.
- [33] O. M. Parkhi, A. Vedaldi, A. Zisserman, and C. V. Jawahar. Cats and dogs. In *IEEE Conference on Computer Vision and Pattern Recognition*, 2012.
- [34] V. Petsiuk, A. Das, and K. Saenko. Rise: Randomized input sampling for explanation of black-box models. *arXiv preprint arXiv:1806.07421*, 2018.
- [35] Z. Qi, S. Khorram, and F. Li. Visualizing deep networks by optimizing with integrated gradients. In *CVPR Workshops*, volume 2, pages 1–4, 2019.
- [36] T. Rojat, R. Puget, D. Filliat, J. Del Ser, R. Gelin, and N. Díaz-Rodríguez. Explainable artificial intelligence (xai) on timeseries data: A survey. *arXiv preprint arXiv:2104.00950*, 2021.
- [37] H. R. Roth, L. Lu, A. Farag, H.-C. Shin, J. Liu, E. B. Turkbey, and R. M. Summers. Deeporgan: Multi-level deep convolutional networks for automated pancreas segmentation. In *Medical Image Computing and Computer-Assisted Intervention–MICCAI 2015: 18th International Conference, Munich, Germany, October 5-9, 2015, Proceedings, Part I 18*, pages 556–564. Springer, 2015.
- [38] O. Russakovsky, J. Deng, H. Su, J. Krause, S. Satheesh, S. Ma, Z. Huang, A. Karpathy, A. Khosla, M. Bernstein, A. C. Berg, and L. Fei-Fei. Imagenet large scale visual recognition challenge, 2015.
- [39] R. R. Selvaraju, M. Cogswell, A. Das, R. Vedantam, D. Parikh, and D. Batra. Grad-cam: Visual explanations from deep networks via gradient-based localization. In *Proceedings of the IEEE international conference on computer vision*, pages 618–626, 2017.
- [40] A. Shrikumar, P. Greenside, A. Shcherbina, and A. Kundaje. Not just a black box: Learning important features through propagating activation differences. *arXiv preprint arXiv:1605.01713*, 2016.

- [41] K. Simonyan, A. Vedaldi, and A. Zisserman. Deep inside convolutional networks: Visualising image classification models and saliency maps. *arXiv preprint arXiv:1312.6034*, 2013.
- [42] X. Situ, I. Zukerman, C. Paris, S. Maruf, and G. Haffari. Learning to explain: Generating stable explanations fast. In *NAACL*, pages 5340–5355, 2021.
- [43] J. T. Springenberg, A. Dosovitskiy, T. Brox, and M. Riedmiller. Striving for simplicity: The all convolutional net. *arXiv preprint arXiv:1412.6806*, 2014.
- [44] M. Sundararajan, A. Taly, and Q. Yan. Axiomatic attribution for deep networks. In *International conference on machine learning*, pages 3319–3328. PMLR, 2017.
- [45] E. Tjoa and C. Guan. A survey on explainable artificial intelligence (xai): Toward medical xai. *IEEE transactions on neural networks and learning systems*, 32:4793–4813, 2020.
- [46] B. Vandersmissen and J. Oramas. On the coherence of quantitative evaluation of visual expalantion. *arXiv preprint arXiv:2302.10764*, 2023.
- [47] Y. Wang. Causal class activation maps for weakly-supervised semantic segmentation. In *UAI 2022 Workshop on Causal Representation Learning*, 2022.
- [48] O. Zaidan, J. Eisner, and C. Piatko. Using “annotator rationales” to improve machine learning for text categorization. In *Human language technologies 2007: The conference of the North American chapter of the association for computational linguistics; proceedings of the main conference*, pages 260–267, 2007.
- [49] M. D. Zeiler and R. Fergus. Visualizing and understanding convolutional networks. In *Computer Vision—ECCV 2014: 13th European Conference, Zurich, Switzerland, September 6-12, 2014, Proceedings, Part I 13*, pages 818–833. Springer, 2014.
- [50] D. Zhang, H. Zhang, J. Tang, X.-S. Hua, and Q. Sun. Causal intervention for weakly-supervised semantic segmentation. *Advances in Neural Information Processing Systems*, 33:655–666, 2020.
- [51] B. Zhou, A. Khosla, A. Lapedriza, A. Oliva, and A. Torralba. Learning deep features for discriminative localization, 2015.
- [52] B. Zhou, A. Lapedriza, A. Khosla, A. Oliva, and A. Torralba. Places: A 10 million image database for scene recognition. *IEEE Transactions on Pattern Analysis and Machine Intelligence*, 2017.

## Appendix

### API tutorial

In the supplementary material, we provide a tutorial on how to utilize our developed user-friendly API, powered by the xaibenchmark Python library. This tutorial guides users through the process of automatically loading our proposed dataset and conducting evaluations of visual explanation methods against our ground truth annotations, as shown in Figure. 4 and Figure. 5, respectively. For more detailed tutorials, please visit <https://xaidataset.github.io>.

```
import xaibenchmark

dataset = "pascal"
class_list = "aeroplane,bicycle,boat,bus"

train_dataloader, val_dataloader, test_dataloader = xaibenchmark.loading(dataset, class_list)

print("Show output size:")
for batch_id, (images, attentions, class_ids) in enumerate(train_dataloader):
    print(images.shape)
    print(attentions.shape)
    print(class_ids.shape)
    break
```

✓ 7.4s

Loading data...  
Splitting dataset...  
Creating dataloaders...  
Data loading complete.  
Show output size:  
torch.Size([32, 3, 224, 224])  
torch.Size([32, 224, 224])  
torch.Size([32])

Figure 4: Loading proposed datasets

```
import numpy as np
import xaibenchmark

# Generate random explanation maps and ground truths
num_samples, image_height, image_width = 16, 224, 224
maps = np.random.rand(num_samples, image_height, image_width)
gts = np.random.randint(0, 2, (num_samples, image_height, image_width))

iou_value = xaibenchmark.iou(maps, gts)
precision_value = xaibenchmark.precision(maps, gts)
recall_value = xaibenchmark.recall(maps, gts)
pointing_game = xaibenchmark.hit(maps, gts)

print("IoU: ", iou_value)
print("Precision: ", precision_value)
print("Recall: ", recall_value)
print("Pointing Game: ", pointing_game)
```

✓ 0.0s

IoU: 0.5001444913903061  
Precision: 0.5001444913903061  
Recall: 0.4994970690132209  
Pointing Game: 0.375

Figure 5: Evaluation APIs

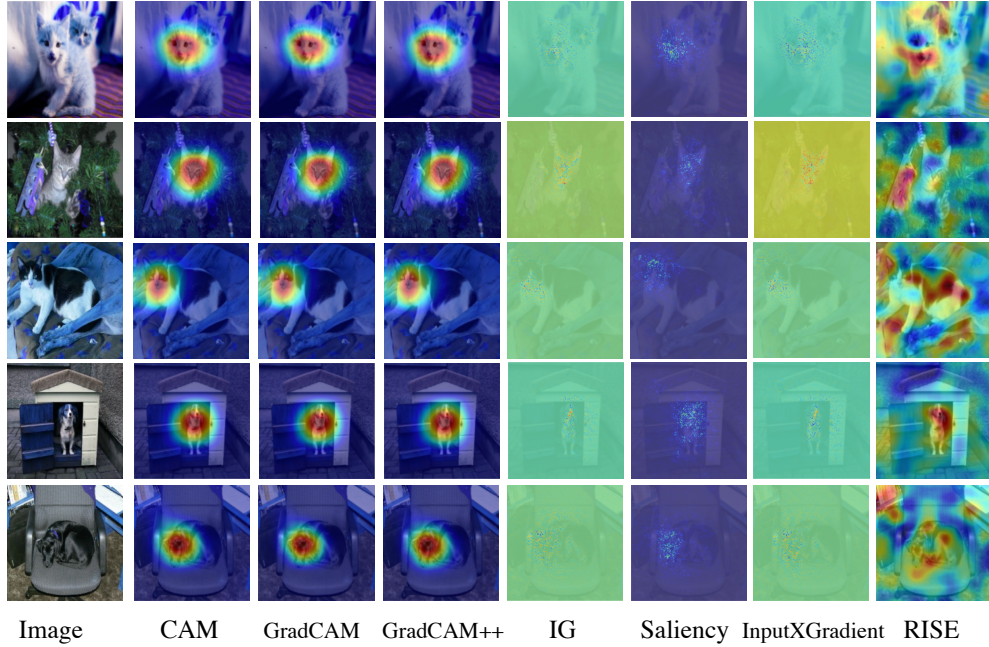


Figure 6: Qualitative Evaluation of Selected Explanation Methods

### Qualitative Analysis

As shown in Figure 6 in the supplementary section, we conduct qualitative analysis on selected examples of the Cat and Dog dataset and provide visualizations of eight explanation methods discussed above, evaluating the performance of different types of explanation methods (gradient-based, perturbation-based, CAM-based, and etc). Overall, gradient-based methods generate sparsely scattered explanations, while other methods generate more coarse heatmaps that are more intuitive to human understanding. Yet all methods seem to perform well at highlighting the most important region of the image, namely the cat or the dog. We observe that CAM-based methods (CAM, GradCAM, GradCAM++) generally exhibit similar behavior when producing the saliency map. These types of methods generally perform well at locating the important region, yet the heatmap is slightly coarse compared with other methods. RISE produces more fine-grained heatmaps at the cost of introducing non-important regions. For example, in Row 4, CAM-based methods generate a circle-shaped importance map that not only highlights the dog but also its surroundings. While RISE is more successful at outlining the dog shape, it may highlight non-important regions more occasionally, as shown in Row 1, 2, 3, and 5. These examples explain why these explanation methods have low precision yet high recall. RISE has higher recall over CAM-based methods since it performs better at capturing the actual shape of the important area. In addition, we observe that IG and InputXGradient generate similar explanations, as well as Saliency and GBP. The saliency maps generated by IG and InputXGradient are more scattered than those generated by Saliency and GBP.

### Inter-method reliability

Inter-method reliability [46] examines if two metrics define the quality of an explanation similarly. To gauge this, we compute a correlation score. For two methods yielding continuous values, we employ the Spearman rank correlation. If one method gives binary outcomes (like the Pointing Game) and the other offers continuous values, the point-biserial correlation is used. When metrics have opposing rank preferences (one preferring higher values and the other lower), we standardize their orderings for the Spearman correlation since it focuses on rank rather than actual values.

We selected three visual explanation methods for our inter-method reliability analysis: GradCAM (a CAM-based method), IG (a Gradient-based method), and RISE (a Perturbation-based method). We

evaluated these methods using four metrics: two performance-based metrics (IoU and Pointing) and two causality-based metrics (insertion and deletion).

The computed correlation results can be observed in Table 4. For GradCAM and IG, the insertion and deletion metrics demonstrate a pronounced negative correlation. This suggests that explanations scoring high in insertion tend to score low in deletion. This behavior underscores that these two metrics possess divergent views regarding the quality of an explanation. In contrast, for RISE, the insertion and deletion metrics do not manifest a robust negative correlation. One plausible rationale is that, since RISE is also perturbation-based, both insertion and deletion yield favorable outcomes, leading to a muted correlation. Furthermore, there is a pronounced negative correlation between the deletion and pointing metrics. A noteworthy observation is the consistent sign of the correlation and the proximity of absolute values for GradCAM and RISE, which is not the case with IG. We posit that this discrepancy with IG is attributable to the dispersed nature of the explanations it generates.

Correlation coefficients	GradCAM	IG	RISE
Insertion & Deletion	-0.5	-0.3	0.1
Insertion & Pointing	0.6	0.1	0.3
Insertion & IoU	0.7	0.3	0.3
Deletion & Pointing	-0.9	-0.6	-0.9
Deletion & IoU	-0.8	-0.2	-0.6
Pointing & IoU	0.9	-0.1	0.7

Table 4: The pairwise Spearman correlation coefficient between different evaluation metrics